Full Text View

Volume 29, Issue 9 (September 1999)

Journal of Physical Oceanography
Article: pp. 2191–2209 | Abstract | PDF (1.25M)

Dynamics of the Eastern Surface Jets in the Equatorial Indian Ocean*

Weiqing Han and Julian P. McCreary Jr.*

Oceanographic Center, Nova Southeastern University, Dania, Florida

D. L. T. Anderson

European Centre for Medium-Range Weather Forecasts, Reading, United Kingdom

Arthur J. Mariano

RSMAS, University of Miami, Miami, Florida

(Manuscript received April 21, 1998, in final form September 23, 1998)

DOI: 10.1175/1520-0485(1999)029<2191:DOTESJ>2.0.CO;2

ABSTRACT

An hierarchy of ocean models is used to investigate the dynamics of the eastward surface jets that develop along the Indian Ocean equator during the spring and fall, the Wyrtki jets (WJs). The models vary in dynamical complexity from 2½-layer to 4½-layer systems, the latter including active thermodynamics, mixed layer physics, and salinity. To help identify processes, both linear and nonlinear solutions are obtained at each step in the hierarchy. Specific processes assessed are as follows: direct forcing by the wind, reflected Rossby waves, resonance, mixed layer shear, salinity effects, and the influence of the Maldive Islands. In addition, the sensitivity of solutions to forcing by different wind products is reported.

Consistent with previous studies, the authors find that direct forcing by the wind is the dominant forcing mechanism of the WJs, accounting for 81% of their amplitude when there is a mixed layer. Reflected Rossby waves, resonance, and mixed layer shear are all necessary to produce jets with realistic strength and structure. Completely new results are that precipitation during the summer and fall considerably strengthens the fall WJ in the eastern ocean by thinning the mixed layer, and that the Maldive Islands help both jets to attain roughly equal strengths.

In both the ship-drift data and the authors' "best" solution (i.e., the solution to the highest model in the authors' hierarchy), the semiannual response is more

than twice as large as the annual one, even though the corresponding wind components have comparable amplitudes. Causes of this difference are as follows: the complex zonal structure of the annual wind, which limits the directly forced response at the annual frequency;resonance with the semiannual wind; and mixed layer shear flow, which interferes constructively (destructively) with the rest of the response for the semiannual (annual) component. Even in the most realistic solution, however, the annual component still weakens the fall WJ and strengthens the spring one in the central ocean, in contrast to the ship-drift data; this model/data discrepancy may result from model deficiencies, inaccurate driving winds, or from windage errors in the ship-drift data themselves.

1. Introduction

a. Observations

Ship-drift climatology indicates that the surface currents in the equatorial Indian Ocean reverse direction four times a year, flowing westward during the winter, weakly westward in the central and western ocean during the summer, and strongly eastward during the spring and fall (Fig. 1a; after Mariano et al. 1995). The eastward currents were first pointed out by Wyrtki (1973), and they are now commonly referred to as Wyrtki jets (WJs), a convention that we follow throughout this paper. Note that the two WJs have roughly the same strength, with the fall one (100 cm s^{-1}) being somewhat stronger than the spring one (90 cm s^{-1}). (The data have been smoothed as described in the caption to Fig. 1. Maximum speeds of the unsmoothed data can exceed 120 cm s^{-1}). Direct current measurements at Gan Island (0.5°S, 73°E) support this result, showing that the fall jet in 1973 (102 cm s^{-1}) was somewhat stronger than either the preceding or following spring jets (94 and 84 cm s^{-1}) (Knox 1976; McPhaden 1982). Other data, however, suggest that one or the other of the two jets is significantly stronger. For example, drifter climatology indicates that the fall jet (75 cm s^{-1}) is stronger than the spring one (50 cm s^{-1}) at 70°E (Molinari et al. 1990). Conversely, geostrophic calculations based on the Tropical Ocean Global Atmosphere (TOGA) World Ocean Circulation Experiment (WOCE) XBT data of 1986–89 indicate that the spring jet had greater transport than the fall one near 80°E (Donguy and Meyers 1995). Such differences are expected from short data records, given that the WJs exhibit significant interannual variability (Knox 1976; McPhaden 1982; Anderson and Carrington 1993; Reppin et al. 1998). Currently, then, the ship-drift observations are the only dataset that is long enough to estimate a reliable WJ climatology.

The total currents in Fig. 1 are dominated by contributions from their time-averaged mean, annual, and semiannual Fourier components (>85%). The mean flow is eastward in the interior ocean, attaining a maximum speed of 32 cm s^{-1} at 80°E. The maximum amplitude of the annual component occurs at the western boundary due to the annually reversing Somali Current, but there is also a significant relative maximum (25 cm s^{-1}) in the central ocean. The maximum amplitude of the semiannual component occurs in the central ocean (70 cm s^{-1}), and is nearly three times as strong as the annual component there. Higher-frequency contributions do not have an organized structure, and hence appear to be noise. Their contribution to the total current, however, is not insignificant. For example, a superposition of the mean, annual, and semiannual components in Fig. 1 produces a fall WJ that is about 30 cm s^{-1} stronger than the spring one; it is the higher-frequency components (primarily the 4-month variability) that eliminate this tendency.

Like the currents, the climatological equatorial zonal wind stress is also dominated by its time-averaged mean, annual, and semiannual components [Fig. 2; based on 1970–96 Florida State University (FSU) monthly mean winds; Legler et al. (1989)]. The mean wind is eastward in the ocean interior and has an amplitude of 0.3 dyn cm^{-2} at 80°E. The maximum amplitude of the annual component (Fig. 2c) is located near the western boundary, and is associated with the monsoon winds off Somalia. There are also two relative maxima centered near 82°E and near the eastern boundary, due to monsoon winds extending southward from the east coast of India and along Indonesia, respectively. The semiannual component has westerlies in the spring and fall during the transition seasons between the two monsoons, and it has a simple structure with a single maximum located in midocean. Presumably, these two wind components drive the corresponding current fields in Fig. 1. It is noteworthy, then, that the oceanic response is so strongly dominated by the semiannual component, even though the two wind components have roughly equal amplitudes in the interior ocean.

b. Dynamical background

Idealized modeling studies and data analyses have suggested the importance of several processes in WJ dynamics. These processes include direct forcing by the wind, propagating waves, mixed layer shear, and resonance.

In his original paper, Wyrtki (1973) suggested that the eastward jets were directly forced by the equatorial westerlies between the two monsoons. Shortly thereafter, O'Brien and Hurlburt (1974) used a two-layer model to demonstrate theoretically that a strong eastward jet does develop as a direct response to switched-on westerlies. They also noted that Rossby waves reflected from the eastern boundary of their model basin were an important part of the response, tending to cancel the directly forced eastward jet two months after the wind onset. The analyses of Knox (1976) and McPhaden (1982), based on a current record obtained near Gan Island (0°41′S, 73°10′E), confirmed the importance of direct wind forcing. Knox (1976) determined further that the pressure gradient term was a significant part of the zonal momentum balance at Gan, indicating the importance of remote forcing by propagating equatorially trapped waves. McPhaden (1982) later noted the presence of signals with vertical phase propagation there, an almost certain indicator of wave propagation.

Cane (1980) studied equatorial currents using a 1½-layer model with a constant-thickness mixed layer embedded in the active layer. Wind-driven surface jets were strengthened in his solutions, essentially by concentrating them within the thinner mixed layer. Reverdin (1987) reached the same conclusion in his study of Indian Ocean annual variability. He utilized a continuously stratified, linear model in which the mixed layer was parameterized as a region of constant density at the top of a prescribed background density profile. The WJs were stronger when this region was thinner.

As noted above, reflected Rossby waves weaken the directly forced interior jet when the wind is switched on. When the wind is periodic, however, the Rossby waves can *enhance* the interior flow if the wind, and hence the directly forced jet, reverse direction by the time the reflected waves propagate back into the interior ocean. Indeed, Cane and Sarachik (1981) demonstrated that a single baroclinic mode can resonate with the forcing in this way. Let $\mathcal{T}$ be the forcing period, L be the basin width, and c_n be the Kelvin wave speed of the nth baroclinic mode. Then, the response is resonant when

$$\mathcal{T} = \frac{4L}{mc_n}, \qquad (1)$$

where m is a positive integer. According to (1), resonance occurs when $\mathcal{T}$ equals a multiple (m) of the time it takes a Kelvin wave to cross the basin (L/c_n) and a first-meridional-mode (l = 1) Rossby wave to return ($3L/c_n$). [Also see Cane and Moore (1981), who obtained an elegant closed expression for such a resonant mode.] Jensen (1993) argued that resonance of this sort involving the n = 2 baroclinic mode accounted for the relatively large amplitude of the semiannual response in his 3½-layer, Indian Ocean model.

There are now a number of models forced by realistic winds that can simulate circulations throughout the Indian Ocean quite well. Typically, however, these solutions have fall WJs that are weaker than the spring ones, particularly in the eastern ocean. For example, in Jensen's (1993) solution to a 3½-layer model, the fall WJ is weaker than the spring one by about a third (see his Figs. 4, 5, and 6). In McCreary et al.'s (1993; henceforth MKM)[1] solution to a 2½-layer model, the strength of the fall jet is typically only 20 cm s^{-1} or less east of 60°E. In Anderson et al.'s (1993) GCM solution, the maximum speed of the spring jet is greater than 120 cm s^{-1}, whereas that for the fall one is only about 70 cm s^{-1}. In Vinayachandran's (1995) GCM solution, the spring and fall maxima are 113 cm s^{-1} and 95 cm s^{-1}, respectively, but the fall one is unrealistically weak in the eastern ocean.

c. Present research

The goals of this study are to isolate and to quantify the processes that determine the WJs. Specifically, we wish to assess how much each of the processes noted above (i.e., direct wind forcing, reflected Rossby waves, mixed layer shear, and resonance) contributes to WJ strength. We also investigate the sensitivity of solutions to salinity variations (which affect mixed layer thickness), the presence of the Maldive Islands (that can block equatorially trapped waves), and forcing by different wind products. Finally, we seek to explain why the semiannual currents dominate the annual ones in the central basin, and why the spring jet tends to be stronger than the fall one in models.

For these purposes, we utilize a hierarchy of models that range in complexity from 2½-layer to 4½-layer systems, the latter including active thermodynamics, mixed layer physics, salinity variability, and the Maldives. Our approach is to progress from simpler to more complex systems, introducing processes in an orderly manner in order to produce a solution that simulates the WJs in the ship-drift climatology as closely as possible.

2. The ocean models

The models used are nonlinear and linear, 2½-layer, 3½-layer, and 4½-layer systems. The nonlinear ones are all similar to the model used by MKM, differing primarily in the inclusion of additional layers and salinity, and the linear ones are similar to the model used by McCreary et al. (1996, henceforth MHSS). Here, then, we provide only an overview of the models,

focusing on aspects that differ significantly from the MKM and MHSS systems.

a. Structures

Figure 3 illustrates the vertical structure of the nonlinear, 4½-layer model. It consists of four dynamically active layers with velocities $\mathbf{v}_i = (u_i, \upsilon_i)$, layer thicknesses h_i, temperatures T_i, and salinities S_i (i = 1, 2, 3, 4 is a layer index), overlying a deep inert ocean with temperature T_d = 3°C and salinity S_d = 34.8 psu. The density of each layer is

$$\rho_i = \rho_0(1 + \alpha_t T_i + \alpha_s S_i), \quad (2)$$

where ρ_0 = 1 g cm^{-3} is a typical oceanic density, and $\alpha_t = -2.5 \times 10^{-4}$ °C^{-1}, and $\alpha_s = 8 \times 10^{-4}$ psu^{-1} are coefficients of thermal and salinity expansion. The layers correspond to either distinct oceanic regions or water-mass types: Layer 1 is the surface mixed layer, layer 2 is the region between the mixed layer and the thermocline (essentially the seasonal thermocline; MKM's"fossil" layer), layer 3 is the thermocline, and layer 4 is upper-intermediate water. Fluid is allowed to transfer between layers 1 and 2 and between layers 2 and 3 at velocities w_1 and w_2, respectively, but no mass exchange is allowed across the other interfaces. The systems are thermodynamically active in that T_i, S_i, and ρ_i vary horizontally in response to surface heat and buoyancy fluxes, horizontal advection, entrainment, and detrainment. Finally, h_1 and h_2 are not allowed to become thinner than minimum values $h_{1\min}$ = 20 m and $h_{2\min}$ = 10 m. These minima are necessary to keep the model numerically stable, and solutions are not sensitive to their values provided they are sufficiently small. For example, there are no significant differences between solutions with $h_{1\min}$ = 20 m and 10 m, but the WJs are 10%–15% weaker when $h_{1\min}$ is increased to 35 m.

To ensure that SST does not become too cold in strong upwelling regions (like off Somalia), the density of the layer-3 water that entrains into layer 2 is not ρ_3, but rather

$$\rho_e = \rho_0(1 + \alpha_t T_e + \alpha_s S_3), \quad (3)$$

where $T_e = \mathrm{SST}_{\min}(y) - 3$°C and $\mathrm{SST}_{\min}(y)$ is the minimum value of observed SST along any latitude line y (see MKM, p. 187). This specification of ρ_e simulates the property that warmer water at the top of the thermocline entrains into layer 2, rather than water with the average layer temperature T_3.

The 3½-layer model differs from the 4½-layer one in that velocity shear between layers 1 and 2 is not allowed. It is obtained from the 4½-layer model by setting $\rho_1 = \rho_2 = \bar{\rho}$ in the pressure gradient fields, $u_1 = u_2 = \bar{u}$, and $\upsilon_1 = \upsilon_2 = \bar{\upsilon}$, where $\bar{q} = (q_1 h_1 + q_2 h_2)/(h_1 + h_2)$. The resulting system consists of three dynamically independent layers, with a thermodynamic mixed layer imbedded in the upper active layer. The 2½-layer model is like the 3½-layer one, except that layer 4 is dropped. It is obtained from the 3½-layer code simply by setting $S_4 = S_d$ and $T_4 = T_d$. This system is most similar to the MKM model, differing only in the specification of w_1 and that $h_{2\min} \neq 0$. Because of the hierarchical arrangement of our solutions, salinity effects are excluded from the 2½-layer and 3½-layer models; this is accomplished by setting $\alpha_s = 0$.

Linear models are also used, because it is possible to separate their solutions into vertical modes and into directly forced and reflected-wave parts. They are obtained by linearizing the nonlinear ones about a state of rest in which background layer thicknesses, temperatures, and salinities are set to constant values, H_i, T^*_i, and S^*_i, and by setting $w_1 = w_2 = 0$.

b. Across-interface velocities

The across-interface velocities, w_1 and w_2, are a crucial part of the physics of the nonlinear models, as they determine all their vertical-mixing processes. They are represented as the sum of various processes by

$$w_1 = w_k + w_r + w_{1c} + \epsilon w_s \equiv w_1' + \epsilon w_s, \quad (4a)$$

$$w_2 = w_s + w_{2c} + \epsilon w_1'^{+}. \quad (4b)$$

For our purposes, the key process in these equations is w_k, which specifies the entrainment into, and detrainment from,

the mixed layer. Velocity w_s parameterizes subduction of layer-2 water into layer 3, a process that is important primarily in the southern Indian Ocean; it is specified as in Eq. (7) of MKM except that here w_s is set to zero within 5° of the equator. Velocity w_r is a correction term that increases h_1 until it is thick enough for the bulk Richardson number of layer 1 to be greater than or equal to ¼; it is needed only to keep the solution stable along the Somali coast where the current becomes very strong during the southwest monsoon. Terms w_{1c} and w_{2c} ensure that h_1 and h_2 never become thinner than their minimum thicknesses. The remaining two terms are proportional to the switch function ϵ, defined by $\epsilon = 1$, if $h_2 = h_{2\min}$, and $\epsilon = 0$, otherwise. They ensure that when $h_2 = h_{2\min}$ (so that layer 2 is essentially not there), layer-1 entrainment, $w'^{+}_1 = \max(w'_1, 0)$, acts at the bottom of layer 2 and subduction w_s acts at the bottom of layer 1.

Velocity w_k is determined by Kraus–Turner (1967) physics according to

$$w_k = \begin{cases} \dfrac{P}{\frac{1}{2}gh_1\Delta\rho'}, & P > 0 \\ \dfrac{h_{\mathrm{mo}} - h_1^-}{2\Delta t}, & P \le 0, \end{cases} \qquad (5a)$$

where

$$P = mu_*^3 - \frac{1}{2}gh_1[-\alpha_t Q - \alpha_s(\mathcal{E} - \mathcal{P})S_1] \qquad (5b)$$

is the production of turbulent kinetic energy;

$$\Delta\rho' = \begin{cases} \rho_2 - \rho_1 + \delta\rho, & h_2 > h_{2\min} \\ \rho_e - \rho_1, & h_2 = h_{2\min}, \end{cases} \qquad (5c)$$

is the density jump at the base of the mixed layer; and

$$h_{\mathrm{mo}} = \frac{mu_*^3}{\frac{1}{2}g[-\alpha_t Q - \alpha_s(\mathcal{E} - \mathcal{P})S_1]} \qquad (5d)$$

is the Monin–Obukhov depth. In these equations, h^-_1 is the layer-1 thickness at the previous time level, Δt is the model time step, Q is the net surface heating, $\mathcal{E} - \mathcal{P}$ is evaporation minus precipitation, $u*$ is the oceanic friction velocity, $m = 1$ is the wind-stirring coefficient, and $g = 980$ cm s^{-2} is the acceleration of gravity. The term $\delta\rho = 2.5 \times 10^{-7}$ g cm^{-3} is included in (5c) only to ensure that the denominator of (5a) never vanishes, and it otherwise does not influence the solution. According to (5a), layer 1 entrains water from layer 2 when $P > 0$, and detrains instantly (i.e., in one time step of the integration) to the Monin–Obukhov depth h_{mo} when $P \leqslant 0$. According to (5c), if h_2 is at its minimum thickness $h_{2\min}$, layer 1 will entrain water of density ρ_e from layer 3.

c. Boundary conditions, forcing, and numerics

The model basin resembles that of the actual Indian Ocean north of 29°S, and is shown in many figures of MKM. For the solutions discussed in section 3d, the basin includes a representation of the Maldive Islands consisting of two parts, the main island chain defined by the rectangular region 2°–6°N, 73°–74°E and Suvadiva Island represented by the single grid box centered at 0.75°N, 73.25°E. Basin and island boundaries are vertical walls, and no slip boundaries are applied there.

The southern boundary is open; zero-gradient boundary conditions with a damper on u_i are applied there (see MKM),

except for the thermocline layer (layer 3) for which water that enters the basin has a temperature of 15°C and a salinity of 35.6 psu. Because the southern boundary is open, two correction "wedges" are included in the southwestern corners of the basin to ensure that mass is conserved (see MKM). One of them, located in layer 3, ensures that mass is conserved in layers 1, 2, and 3; the other, located in layer 4, ensures that mass is conserved in layer 4.

Unless specified otherwise, the wind stress, $\boldsymbol{\tau} = \rho_a C_D |\mathbf{V}|\mathbf{V}$, used to force the model is the FSU monthly mean pseudostress $|\mathbf{V}|\mathbf{V}$ averaged from 1970 to 1996 (Legler et al. 1989), with ρ_a = 0.001 175 g cm^{-3} and C_D = 0.0015. In addition, monthly climatological fields of air temperature T_a, specific humidity, incoming solar radiation Q_r, outgoing longwave radiation, and scalar wind w_{sc} derived by Rao et al. (1989, 1991) are used to obtain the surface heat fluxes. The fluxes are determined from standard bulk formulae, using model SST (T_1) in the calculation for the sensible and latent heat fluxes (McCreary and Kundu 1989; MKM). Precipitation P is provided by Legates and Willmott (1990).

The oceanic friction velocity $u*$ in (5b) is determined from w_{sc} according to $u* = \gamma^{1/3}(C'_D(\rho_a/\rho_0))^{1/2} w_{sc}$, where C'_D = 0.0014, $\gamma(w_{sc}) = 1 + [1 - (w_{sc}/w_{cr})^3]\theta(w_{cr} - w_{sc})$, θ is a step function, and w_{cr} = 5 m s^{-1}. Coefficient γ is a factor that strengthens $u*$ at low wind speeds. We estimated its form using a year-long record of wind data from the central Arabian Sea (Weller et al. 1998).

For the nonlinear models, solutions are obtained by directly integrating the equations of motion for each layer. For the linear models, solutions are represented as expansions in vertical normal modes. In this case, equations of motion for each mode [like Eq. (3) in MHSS] are integrated numerically, and the total response is then the sum over the solutions for each mode. The modal decomposition requires calculating characteristic speeds c_n and coupling thicknesses $\mathcal{H}_n$ for each mode. They are determined from the stratification parameters, H_i, T^*_i, and S^*_i, which are specified to be annual-mean zonally averaged values of h_i, T_i, and S_i along the equator from a corresponding nonlinear solution. The forcing of each mode is $\boldsymbol{\tau}/\mathcal{H}_n$, so that the nondimensional coefficient $\Phi_n = \mathcal{H}/\mathcal{H}_n$, $\mathcal{H}$ = 100 m, measures how effectively each mode couples to the wind. Table 1 lists values of H_i, T^*_i, S^*_i, c_n, and Φ_n for each of the linear models.

Solutions are obtained on a grid of dimension $\Delta x = \Delta y$ = 55 km, and are integrated forward in time with a time step of Δt = 1 h for all the models, except for the nonlinear, 4½-layer model for which Δt = 0.8 h. For the nonlinear models, both biharmonic and Laplacian mixing are included in all equations to control noise. The biharmonic coefficient is 10^{21} cm^4 s^{-1}, the Laplacian coefficients for momentum and temperature are 5×10^7 cm^2 s^{-1}, and those for salinity and layer thickness are 10^7 cm^2 s^{-1}. For the linear models, only Laplacian mixing on momentum is included.

All solutions are spun up from a state of rest beginning on 15 April. For the nonlinear solutions, initial values for temperatures are T_1 = observed SST from Rao et al. (1989, 1991), $T_2 = T_e$, T_3 = 15°C, and T_4 = 9°C, those for salinity are $S_1 = S_2$ = sea surface salinity from Levitus and Boyer (1994) data, S_3 = 35.4 psu, and S_4 = 35 psu, and those for layer thicknesses are H_1 = 35 m, H_2 = 30 m, H_3 = 300 m, and H_4 = 400 m. Solutions are integrated for a period of 10 years and all figures shown are from year 9 to 10.

3. Results

In this section, we present a hierarchy of solutions designed to isolate the processes that determine the WJs. Specifically, in section 3a we discuss solutions to the 2½-layer models, pointing out influences of direct forcing by the wind, reflected Rossby waves, and nonlinearities. In section 3b, we discuss solutions to the 3½-layer models, which have a near-resonant response due to the addition of the subthermocline layer. In section 3c, we report solutions to the 4½-layer models, which include a surface mixed layer. Finally, in sections 3d and 3e we report on the sensitivity of solutions to the Maldive Islands and to forcing by different wind products. To help understand solution properties and to identify key processes, at each step in the hierarchy we obtain solutions to both the linear and nonlinear models.

a. Solutions to the 2½-layer models

1) NONLINEAR SOLUTION

Figure 4 shows x–t plots of u_1 averaged from 1°S to 1°N for the solution to the nonlinear, 2½-layer model (Fig. 4a

), as well as its mean (Fig. 4b), annual (Fig. 4c), and semiannual (Fig. 4d) components. Both WJs are somewhat weaker than the observed ones, attaining maximum speeds of 84 cm s^{-1} and 83 cm s^{-1} during the spring and fall, respectively (compare Figs. 1a and 4a). The fall WJ, however, is much weaker throughout the eastern ocean, with a distinct relative minimum near 75°E that is not present in the observations. A striking feature is a summertime velocity front that terminates the spring WJ; it develops near 85°E in May, propagates westward at a speed of 36 cm s^{-1}, and dissipates near 65°E in August. A similar wintertime front terminates the fall WJ in the western ocean.

The overall structure of the response is captured by its mean, annual, and semiannual components. The mean flow strengthens from east to west, a structure quite different from that of the observed annual mean (Fig. 1b). Isotachs tilt upward to the west for the annual component, again in contrast to the observations that have little or no tilt (Fig. 1c). The structure of the semiannual component resembles that of the data, but its amplitude (46 cm s^{-1}) is considerably weaker (Fig. 1d);nevertheless, it is still nearly twice as strong as the annual component (26 cm s^{-1}). Higher-frequency contributions (not shown) act primarily to sharpen the velocity fronts. They also tend to increase current speeds in the vicinity of the fronts, intensifying the WJ maxima somewhat. For example, when only the mean, annual, and semiannual components are superposed, the maximum speeds of the spring and fall WJs are 79 and 67 cm s^{-1}.

2) LINEAR SOLUTION

To isolate effects due to direct wind forcing and reflected waves, we obtained two solutions to the linear, 2½ layer model, one with and the other without a damper in the eastern equatorial ocean. For the solution with the damper, the eastern boundary of the basin is extended to 115°E, and there is no forcing in this extended area. The damper is applied in the region $x > 107.5°$E, $-7.5° < y < 7.5°$, and it relaxes the zonal-velocity and pressure fields of each mode to zero there (see MHSS for details). It efficiently absorbs equatorial Kelvin waves so that almost no Rossby waves reflect from the eastern boundary back into the ocean interior. Thus, the damped solution is the part of the total (i.e., undamped) solution that is *independent of* reflected Rossby waves, and we refer to it as the "forced" response. (With this definition, the forced response includes effects due to Kelvin waves reflected from the western boundary. Nevertheless, it still is a useful measure of the part of the solution that is directly forced by the wind.) Conversely, the *difference* between the undamped and damped solutions is the part that is generated by Rossby waves reflected from the eastern boundary, and we refer to it as the "reflected wave" response.

Figure 5a shows the undamped (total) solution that corresponds to the nonlinear solution in Fig. 4 . Generally, the two solutions are similar except for a few explainable differences discussed in sections 3a(4) and 3b(5), and this good agreement gives us confidence that conclusions based on the linear solution also apply to the nonlinear one. Figure 5b shows the annual and semiannual components of the directly forced (panels a and c) and reflected-wave (panels b and d) parts of the solution in Fig. 5a . According to the above definitions, it is also possible to split the mean component into directly forced and reflected-wave parts. They are not shown because the reflected-wave part is negligible so that the mean response in Fig. 5a is well approximated by the directly forced part.

(i) Forced response

As for the nonlinear solution, the mean current increases westward. This is because the mean circulation is close to being in Sverdrup balance, for which u_1 is proportional to the zonal integral of $(\mathrm{curl}\boldsymbol{\tau})_y$. (In the model, the exact balance is prevented by horizontal mixing.) The structure of the annual forced response is rather complex, having a maximum near the western boundary and two relative maxima in the central and eastern ocean [Fig. 5b(a)], a pattern that reflects the complex structure of the annual forcing (Fig. 2c). In contrast, the structure of the semiannual forced response is much simpler, with isotachs having little or no tilt [Fig. 5b(c)]. This simplicity happens because the semiannual winds also have a simple structure, consisting of a single maximum located in the central ocean (Fig. 2d).

(ii) Reflected-wave response

From the isotach tilt, it is evident that the reflected-wave response is largely composed of signals with a westward propagation speed of about 45 cm s^{-1} [Figs. 5b(b) and 5b(d)]. This property identifies them as being primarily $l = 1$, $n = 2$ Rossby waves, which also have a speed of $c_2/3 = 45$ cm s^{-1} (see Table 1). Indeed, the amplitude of the $n = 2$, semiannual reflected-wave contribution is 27.7 cm s^{-1}, whereas that of the $n = 1$ mode is only 5.7 cm s^{-1}. The total semiannual signal appears to propagate somewhat slower in the eastern ocean, largely due to interference with the $n = 1$ waves.

(iii) Interference

For the semiannual component, the reflected waves combine with the forced response to produce a distinct current maximum in the central-eastern ocean, and isotachs tilt slightly upward to the west [Figs. 5a(c) and (d) and 5b(c) and (d)]. For the annual component, however, the isotach tilt of the combination is large throughout the interior ocean [Fig. 5a(c)], significantly more than the tilt associated with a pure $n = 2$ Rossby wave [Figs. 5b(b) and 5b(d)]. Apparently, then, the interference pattern between the annual, forced and reflected-wave responses is sensitive to details of the structures of each part, producing a total pattern that does not much resemble either part by itself. As we shall see, the annual components of the other solutions in our hierarchy also exhibit a similar sensitivity.

3) STRONG SEMIANNUAL COMPONENT

The amplitude of the semiannual component in the linear solution is more than twice as large as the annual one throughout the interior ocean [Figs. 5a(c) and 5a(d)]. As noted in the introduction, this dominance is somewhat surprising given that the wind components have roughly equal amplitudes in the interior ocean (Figs. 2c and 2d).

One cause of this property is direct forcing by the wind since, except for the western-boundary region, the semiannual forced response is more than twice as strong as the annual one [Figs. 5b(a) and 5a(c)]. This property results from the different spatial structures of the semiannual and annual wind components, rather than their different frequencies. To demonstrate this, we obtained a damped solution forced by a wind field with the same spatial structure as the semiannual wind but oscillating at the annual period: The resulting forced response had a zonal structure and amplitude similar to those in Fig. 5b(c). A second cause is that the semiannual, forced and reflected-wave parts interfere constructively at some point along the equator, increasing the total response by almost 20 cm s^{-1}, whereas those for the annual component do not because of its lower frequency. These properties can be seen in Fig. 5b in that positive (and negative) regions of the semiannual, forced and reflected-wave responses overlap over much of the central ocean, but those for the annual ones do not. These reasons also account for the strong semiannual components in the other linear solutions in our hierarchy, and we infer that they do so for the nonlinear solutions as well. A third cause involves flow within the mixed layer, and it is discussed in section 3c(3).

4) WEAK FALL WJ

Note that when the annual and semiannual components of u_1 are superposed for both nonlinear and linear solutions, the annual component interferes destructively with the semiannual flow during the fall, thereby causing the relative minima of total u_1 near 75°E and 64°E, respectively (Figs. 4 and 5a). The linear solution suggests that the weakening results from both the directly forced and reflected-wave parts of the annual component, the former having westward flow during November and the latter causing the relative minimum near 64°E (Fig. 5b).

The annual component tends to weaken the fall WJ in all of our solutions. Interestingly, the structure of this component differs considerably among them. In the 2½-layer solutions discussed here, the isotach tilt in the linear solution is half that in the nonlinear one [Figs. 4c and 5a(c)]. In the solutions with mixed layer shear and the Maldives Islands discussed in sections 3c and 3d, its structure is changed even more (Figs. 8b and 11), and in such a way that it affects the WJ maxima less.

5) NONLINEAR EFFECTS

Finally, a comparison of nonlinear and linear solutions indicates that the summertime velocity front in Fig. 4 is generated by $l = 1$, $n = 2$ Rossby waves reflected from the eastern boundary. Note that *both* the annual and semiannual waves in Fig. 5b change from positive to negative during May near 90°E, so that their combination produces a Rossby wave with the same velocity change as that associated with the front. In the nonlinear solution, this velocity change is subsequently sharpened and slowed (from 45 to 36 cm s^{-1}) by the spring WJ to the west of it, thereby forming the front. (MKM also noted the presence of a similar front in their solution, concluding that it was an $l = 1$, $n = 2$ Rossby wave severely slowed by the spring WJ. They also conjectured that this wave caused the weak fall WJ in the eastern ocean of their solution. This is clearly not the case in our solution, as Fig. 4 shows no connection between the two features.) The other front in Fig. 4 also appears to be a Rossby wave slowed by the fall WJ, but it has no obvious relationship to eastern-boundary reflections. Both velocity fronts occur in the 3½-layer, nonlinear solution, and the spring front is present in the 4½-layer one. They are the most prominent nonlinear features in all of our solutions.

b. Solutions to the 3½-layer models

1) NONLINEAR AND LINEAR SOLUTIONS

Figure 6 shows x–t plots of total, mean, annual, and semiannual components of u_1 along the equator for the solution to

the nonlinear, 3½-layer model. The maximum speed of the spring WJ is 96 cm s^{-1}, considerably stronger than in the 2½-layer solution (Figs. 4a and 6a). The fall WJ maximum speed actually weakens somewhat, but the relative maximum in the eastern ocean strengthens significantly from 36 cm s^{-1} to 45 cm s^{-1}. The mean and annual components are little changed (Figs. 4b, 4c, 6b, and 6c). Thus, the strengthened WJs result mostly from the intensified semiannual component, the amplitude of which increases from 46 to 54 cm s^{-1}.

The corresponding linear solutions are so similar in structure to their 2½-layer counterparts in Figs. 5a and 5b that there is no need to display them. Moreover, the amplitudes of all the annual parts (i.e., the total, forced, and reflected-wave parts) and of the semiannual forced response are also very similar, typically differing by 1 cm s^{-1} or less. The only significant difference between the two linear solutions is that the amplitude of the semiannual component of the 3½-layer solution is larger by 18 cm s^{-1} (73 cm s^{-1} as compared to 55 cm s^{-1}), and this increase is due almost entirely to stronger reflected waves. Of this increase, about 8 cm s^{-1} is due to stronger reflected waves for the $n = 2$ baroclinic mode, and 6 cm s^{-1} results from $n = 3$ reflected waves not present in the 2½-layer model. The remaining 4 cm s^{-1} is due to $n = 1$ reflected waves: they tend to *weaken* the semiannual component in both solutions, and their amplitude is *decreased* in the 3½-layer solution.

2) RESONANCE

The property that only the *reflected-wave part* of the semiannual response strengthens, suggests that resonance may be the cause of the increase. To investigate this possibility, we obtained a series of test runs for a single mode, varying its characteristic speed c_n from 20 to 400 cm s^{-1} every 5 cm s^{-1}. For each solution, forcing was the semiannual component of the FSU winds and the coupling thickness $\mathcal{H}_n$ was fixed to $\mathcal{H}$ = 100 m. Figure 7 plots the resulting maxima of zonal velocity along the equator on 15 November (the date of the fall maximum) for the total currents, $u_{1\max}$ (thick curve), and for the reflected-wave parts, $u'_{1\max}$ (thin curve). The figure also plots equatorial zonal velocity for the reflected-wave parts of each test solution at 78°E, u''_1 (thin-dashed curve), a location near the maximum of the semiannual flow in both the 2½-layer and 3½-layer solutions; this curve is useful for discussing how resonance affects jet strength.

The two solid curves exhibit two distinct peaks: a primary one centered near c_n = 165 cm s^{-1}, and a secondary one near c_n = 95 cm s^{-1}. (The thin-dashed curve has only one peak because maxima of the reflected-wave parts for c_n values centered about 95 cm s^{-1} are localized near 85°E, and so are missed at 78°E.) Note that the peaks do not appear in the difference between the two solid curves (a measure of the directly forced response), which remains relatively constant for all c_n. Therefore, the peaks are associated entirely with the reflected-wave parts, a compelling indication that resonance is their cause.

As mentioned in the introduction, Eq. (1) provides a theoretical criterion for resonance based on the Cane and Sarachik (1981) idealized solution. In our model, the width of the basin at the equator is L = 6327 km. When $\mathcal{T}$ is the semiannual period, (1) yields c_n = 163 cm s^{-1} when $m = 1$, and c_n = 82 cm s^{-1} when $m = 2$, both resonant speeds close to the values determined from Fig. 7. The resonance peaks, however, are much broader than they are in the Cane and Sarachik (1981) solution (see their Fig. 1); this is because our model does not assume the long-wavelength approximation, has a realistic shape, and is viscid. Jensen (1993) obtained a similar suite of solutions but found a smaller resonance speed of 140 cm s^{-1} for the $m = 1$ peak, apparently because his basin width was 8° narrower than ours.

Values of c_2 for the 2½-layer and 3½-layer models are 134 and 162 cm s^{-1}, respectively (Table 1), so that the $n = 2$ mode is closer to the resonance peak in the latter model than it is in the former. Mode-2 contributions to the reflected-wave parts of solutions can be determined from Fig. 7 by the relation $\mathcal{U}_2 = \Phi_2 u''_1(c_2)$; it yields 0.87 × 29 = 25 cm s^{-1} and 0.71 × 47 = 33 cm s^{-1} for the 2½-layer and 3½-layer models, which accounts for the increase in amplitude of the $n = 2$, semiannual component noted above (8 cm s^{-1}). Likewise, the amplitudes of the $n = 3$ and $n = 1$ reflected-wave responses estimated from Fig. 7 are $\mathcal{U}_3 = \Phi_3 u''_1(c_3)$ = 6 cm s^{-1} and $\mathcal{U}_1 = \Phi_1 u''_1(c_1)$ = −6 and −2 cm s^{-1} for the 2½-layer and 3½-layer models, respectively, accounting for the aforementioned amplitude increase due to the $n = 3$ (6 cm s^{-1}) and $n = 1$ (4 cm s^{-1}) semiannual components. We conclude that the semiannual component strengthens in the linear, 3½-layer model because c_2 is shifted closer to the resonance peak and because some of the forcing is shifted from the $n = 1$ mode, which is

well off the resonant peak (c_1 = 323 or 375 cm s^{-1}), to the n = 3 mode, which is much closer (c_3 = 118 cm s^{-1}).

Does a shift toward resonance also account for the strengthening of the WJs in the nonlinear, 3½-layer solution? Such an inference is not straightforward, since it is not possible to separate cleanly the nonlinear solutions into forced and reflected parts. Moreover, properties of reflected Rossby waves can be significantly modified in the nonlinear model [section 3a(5)]. On the other hand, the tilt of the summertime velocity front in Fig. 6 is somewhat less than it is in Fig. 4, indicating an increase in its propagation speed from 36 to 43 cm s^{-1}; this supports the idea that n = 2 Rossby waves *are* propagating faster in the nonlinear, 3½-layer solution, and hence that the n = 2 semiannual response may be closer to the resonance peak. To test this idea further, we carried out a suite of test solutions using the nonlinear, 3½-layer (and 4½-layer) models, by varying T_d from 0°C to 7°C. For each of the solutions, the maximum value of equatorial u_1 for the semiannual components was noted, and a value for c_2 was calculated as for the linear models. These data points are indicated in Fig. 7 by ×'s (and ○'s), and they follow curves similar to the linear, resonance curves.

c. Solutions to the 4½-layer models

1) NONLINEAR SOLUTIONS

Figures 8a and 8b(a) show x–t plots of equatorial u_1 for solutions to the nonlinear, 4½-layer models without and with salinity, respectively. In the solution without salinity, the WJs are 10–20 cm s^{-1} stronger than they are in the 3½-layer solution, attaining maximum speeds during the spring (106 cm s^{-1}) and fall (97 cm s^{-1}) comparable to the observations, but the fall jet is still weak in the eastern ocean. In the solution with salinity, the fall WJ is strengthened by as much as 30 cm s^{-1} in the central and eastern ocean, in much better agreement with the data.

In the latter solution, the mean component differs from those in Figs. 4 and 6, attaining a maximum value near 82° E and decreasing westward, as in the observations [Fig. 8b(b)]. This structural change is significant because the mean maximum is now located near the location of the WJ maxima, and consequently it strengthens the WJs by roughly 25 cm s^{-1}, 13 cm s^{-1} more than it does in the other solutions. The structure of the annual component is also altered considerably, the isotach tilt being absent or reversed in the western ocean, but its amplitude remains nearly unchanged [Fig. 8b(c)]. In contrast, the amplitude of the semiannual component is 15 cm s^{-1} greater than it is in the 3½-layer model, and its structure is changed only in that its maxima are shifted westward by about 10° [Figs. 6d and 8b(d); see section 3c(3)]. (The components for the solution without salinity, not shown, are similar to those in Fig. 8b, differing mostly in that the semiannual amplitude is weaker, and the annual one is stronger, by about 5 cm s^{-1}.)

2) MIXED LAYER SHEAR

Recall that the nonlinear, 4½-layer models differ from the 3½-layer one in that they allow shear between layers 1 and 2 (i.e., between the mixed layer and the seasonal thermocline), which suggests that the strengthened currents in Figs. 8a and 8b result from the directly forced response being concentrated within a shallower layer. In support of this idea, maxima of equatorial $\bar{u}$ (defined in section 2a) for both 4½-layer solutions reduce to values similar to those in the nonlinear, 3½-layer solution. In addition, Fig. 9 plots upper-layer thickness, $h_1 + h_2$, for the 3½-layer solution (Fig. 9a) and h_1 for the two 4½-layer solutions (Figs. 9b and 9c). As expected, a comparison of the thickness and velocity panels among the three solutions shows that currents are stronger in regions where the upper layer is thinner.

The thinning of h_1 is particularly apparent in the nonlinear solution with salinity for the fall WJ, when it is thinner than in the solution without salinity by 50 m over much of the central-eastern ocean (Figs. 9b and 9c). This marked thinning results from precipitation $\mathcal{P}$ during the summer and fall, which reduces or even reverses the production of turbulence P [Eq. (5b)] and increases the density jump at the bottom of layer 1, $\Delta\rho'$. Both of these effects act to decrease w_k [Eq. (5a)], thereby slowing or even reversing entrainment into layer 1. In this way, then, the eastern equatorial Indian Ocean is similar to the western Pacific warm-pool region, where strong precipitation forms a thin surface layer that traps momentum close to the surface (Vialard and Delecluse 1998; Soloviev et al. 1998).

3) LINEAR SOLUTION

The corresponding linear, 4½-layer solutions (not shown) also have much stronger WJs than the linear, 3½-layer solution does. Interestingly, their first three modes sum to produce a response very similar to the linear, 3½-layer solution, a similarity that holds for their mean, annual, and semiannual components as well. Thus, the stronger WJs result from the additional contribution of the n = 4 mode. The vertical structure of the currents associated with the n = 4 mode is described

by the eigenvector ψ_4 = (1.0, −1.04, 0.009, −0.0001) for the solution with salinity, and is essentially the same for the solution without salinity. Note that ψ_4 has appreciable values only in layers 1 and 2 and with opposite signs. Thus, the mode-4 currents generate a shear flow in the upper two layers and have virtually no effect in the deeper layers. In addition, Rossby waves do not exist for this mode because its characteristic speed (c_4 = 23 cm s^{-1}) is so low that even the annual frequency is higher than the Rossby wave high-frequency limit (Moore 1968; McCreary 1985); consequently, the mode-4 response has no reflected-wave part at all, and it is entirely directly forced. These properties provide additional support for the idea that the WJs are stronger in the nonlinear, 4½-layer solutions, simply because the mixed layer allows an additional directly forced, shear flow above the thermocline.

In both the nonlinear and linear solutions, the semiannual component is strengthened considerably by the shear-flow contribution, but the annual one is not. In the linear solution, this happens because contributions from mode 4 and modes 1–3 interfere constructively for the semiannual current, with highs and lows coinciding over much of the basin, whereas they interfere destructively for the annual response. We infer that the difference happens in the nonlinear solution for similar reasons; that is, the additional shear flow interferes constructively only for the semiannual response.

Finally, it is worth mentioning that, although the semiannual component associated with modes 1–3 is virtually unchanged from that in the 3½-layer solution, its modal composition is quite different. In the 4½-layer solution, there is little contribution from mode 3 (Φ_3 = 0.08 for the solution with salinity) and more from mode 2 (Φ_2 increases from 0.71 to 0.91). Therefore, in comparison to the 2½-layer solution, 14 cm s^{-1} of the increase in the total semiannual component (18 cm s^{-1}) results from c_2 being shifted closer to the resonance peak, the remaining 4 cm s^{-1} being due to a weaker n = 1 contribution.

4) COMPARISON TO OBSERVATIONS

Levitus and Boyer (1994) and Levitus et al. (1994) data provides evidence that the mixed layer in the real ocean is thinned by precipitation, much as it is in our model. Figure 10 shows mixed layer thicknesses estimated from the data in two different ways: by the depths where temperature is 1°C less than SST h'_m (Fig. 10a) and where density is 0.000 25 g cm^{-2} greater than the surface density h_m (Fig. 10b). (Note that the density change associated with the temperature criterion is the same as that for the density criterion when α_t = −2.5 × 10^{-4} °C^{-1}.) The two thicknesses differ mostly in the eastern Indian Ocean where h_m is significantly thinner than h'_m throughout the year, particularly during October and November when it is thinner by nearly 50 m. We interpret this difference to indicate the presence of a thin mixed layer of fresher water due to the heavy precipitation in the eastern Indian Ocean, a structure similar to that in the western Pacific (Sprintall and Tomczak 1992; Murtugudde and Busalacchi 1998).

The overall structure of the upper-layer thicknesses in the solutions (Fig. 9) compares favorably with the data, the fields in the upper two and bottom panels of Fig. 9 corresponding to h'_m and h_m, respectively. Even some details agree, with h'_m being thickest in the eastern ocean during June and November, being shallowest during March, and having a band of high thicknesses that extends across the basin during the fall (upper panels of (Figs. 9a and 10a). In addition, salinity reduces the mixed layer thickness the most in the central and eastern ocean during October and November in both the solution and the data (Figs. 9b, 9c, and 10b).

d. Influence of the Maldive Islands

1) NONLINEAR SOLUTIONS

Figure 11a shows x–t plots of equatorial u_1 for a solution to the 4½-layer model with salinity in a basin that includes the Maldives (see section 2c). In contrast to the solution without the Maldives [Fig. 8b(a)], the spring WJ maximum (near 80°E) is weaker by almost 20 cm s^{-1} and the fall maximum (near 65°E) is weaker by about 5 cm s^{-1}. Note also that the spring WJ is weaker everywhere west of the islands (73°E) whereas the fall jet is less affected there.

The general decrease in amplitude of both WJs is caused by the mean and semiannual components (Figs. 11b and 11d), which are weaker than their counterparts in Fig. 8b by about 5 and 10 cm s^{-1}, respectively. Modifications to the relative strength of the jets result from changes in the annual component (Fig. 11c), namely, its reduction in amplitude east of the islands and the time delay of extrema west of the island, which is more than 2 months in the central ocean. Both

of these changes tend to weaken the spring WJ and to strengthen the fall one.

2) LINEAR SOLUTIONS

To help understand how the Maldives influence wave propagation, we obtained a set of solutions to the linear, 4½-layer models with and without the Maldives, forced by the semiannual and annual components of the wind confined either west of 65°E or east of 78°E. The solutions indicate that the islands have little effect on the transmission of Kelvin waves, consistent with the conclusions of Yoon (1981) and Cane and du Penhoat (1982). In contrast, Rossby waves are affected much more, with some energy being reflected and some transmitted. Additionally, in order to pass the Maldives, the portion of an incoming Rossby wave signal north of 2°N must first be channeled to the southern edge of the islands (at least to 2°N) via a western boundary current on their eastern side; as a result, the structure of the transmitted signal is altered significantly.

The influence of the Maldives is particularly striking for the annual component, because they reflect part of the strong, annually reversing flow south of Sri Lanka (the Indian Monsoon Current) back into the eastern ocean along the equator and shift another part to be close to the equator west of the islands. This process accounts for most of the changes in structure of the annual component noted above. Effects of the Maldives are less noticeable for the structure of the semiannual component because the forcing excites low-order Rossby waves that are largely confined to, and symmetric about, the equator. As discussed next, however, they do alter the resonance properties of the system.

To investigate the effect of the islands on resonance, we repeated the series of test runs described in section 3b(2) when the basin included the Maldives. The thick-dashed curve in Fig. 7, $\tilde{u}_{1\max}$, plots maxima of equatorial zonal velocity on 15 November from this series, and so is analogous to $u_{1\max}$ (thick curve in Fig. 7). A comparison of the two curves shows that the Maldives weaken the response near the stronger resonant peak by 13 cm s^{-1}. To check the influence of each part of the Maldives, we also obtained similar series that consisted only of the main island chain and only of Suvadiva Island (see section 2c). With only the main island chain, $\tilde{u}_{1\max}$ is almost unchanged from $u_{1\max}$, and is even somewhat larger near 73°E due to the channeling effect noted above. With only Suvadiva Island, $\tilde{u}_{1\max}$ is less than $u_{1\max}$ but at most by about 5 cm s^{-1}. Thus, both parts of the Maldives reduce resonance but Suvadiva Island does so more strongly, as might be expected since it lies well within the equatorial waveguide.

3) COMPARISON TO SHIP-DRIFT DATA

The total, mean, and semiannual components in the nonlinear solution compare reasonably well with the ship-drift observations (except for their having somewhat weaker amplitudes), but the annual component does not (Figs. 1 and 11). It differs mostly in the eastern ocean where it is almost eliminated by reflected waves, but also in the western ocean where it is shifted in phase by 1 month (Figs. 1c and 11c). This model–data discrepancy may indicate that the locally forced response is underestimated in our solution. Alternatively, it may point toward errors in the ship-drift data: windage error can be as large as 3% of the wind speed (McPhaden et al. 1991), resulting in current-speed errors of the order of 15 cm s^{-1} in the central-eastern ocean. As discussed next, it may also result from inaccuracies in the FSU winds.

e. Forcing by other wind products

All previous solutions have been forced by FSU winds. To explore the sensitivity of our solutions to the driving winds, we obtained two other hierarchies of solutions, similar to the above except forced by monthly mean ECMWF (averaged from 1980 to 1988) and Hellerman and Rosenstein (1983) wind stresses. Both sets lead to the same conclusions about WJ dynamics as discussed above. The strengths of the WJs, however, differ considerably among the three sets: When forced by ECMWF winds, the solution to the 4½-layer model with salinity and the Maldive Islands has a spring WJ of 120 cm s^{-1} at 83°E and a fall jet of 100 cm s^{-1} at 75°E. When forced by Hellerman and Rosenstein (1983) winds, the response has a spring jet of 90 cm s^{-1} at 77°E and a fall jet that is about 75 cm s^{-1} in the central and western ocean, but is unrealistically weak in the eastern ocean. Similar tests have been carried out by Anderson and Carrington (1993) using a 16-level GCM, and they reveal similar sensitivities. In their solution forced by Hellerman and Rosenstein (1983) winds, the fall WJ was considerably weaker than the spring one. When the forcing was by the U.K. Meteorological Office (UKMO) wind product, however, the fall jet was actually somewhat stronger than the spring one. These significant differences emphasize the necessity of improving the accuracy of wind measurements in the equatorial Indian Ocean.

4. Summary and discussion

In this paper, we report an hierarchy of solutions that isolates processes important in WJ dynamics. At each step of the hierarchy we obtain both nonlinear and linear solutions, the latter allowing us to separate solutions into contributions from individual baroclinic modes and into directly forced and reflected-wave parts. Because the wind is dominated by its mean,

annual, and semiannual components (Fig. 2), it is also useful to separate solutions into these frequency components as well. Indeed, these three components contain all the basic jet physics, the higher-frequency ones generally producing localized responses associated with fronts [section 3a(5)]. The next three paragraphs summarize the major conclusions for each frequency component.

All our solutions develop eastward mean currents, in response to the westerly mean winds (Fig. 2b). Their structures, however, change markedly depending on whether the model has a mixed layer. Without a mixed layer, currents increase to the west (Figs. 4b and 6b), essentially a nonlocal, Sverdrup flow proportional to the zonal integral of $(\mathrm{curl}\boldsymbol{\tau})_y$. With a mixed layer, the maximum current occurs near 75°–80°E, in much better agreement with the observations [Figs. 8b(b), 11b, and 1b]. In these solutions, the flow structure is similar to that of τ^x itself (Fig. 2b), an indication that the governing dynamics are predominately local. Moreover, because the location of the mean maximum is now close to the longitude of the WJ maxima, the mean flow contributes considerably more to jet strength (increasing from about 12 to 25 cm s^{-1}).

The structures of the annual components also change markedly among the various solutions. Without a mixed layer, isotachs tilt upward toward the west [Figs. 4c, 5a(c), and 6c]. This tilt is considerably more than that associated with a pure Rossby wave, and hence results from interference between the directly forced and reflected-wave responses. With a mixed layer, the isotach tilt is absent in the western ocean because of the strengthened directly forced response there [Fig. 8b(c)]. With the Maldive Islands, the annual response is almost eliminated in the eastern ocean, and its phase is shifted by more than 2 months in the central ocean (Fig. 11c);as a consequence, the annual component tends to strengthen the spring WJ and to weaken the fall one *less* than it does in the solution without the Maldives, thereby allowing them to have more equal strengths.

The amplitudes of the semiannual components generally strengthen in progressing up the hierarchy, and the linear solutions identify the processes that cause this change. The increase between the 2½-layer and 3½-layer solutions happens because the semiannual, reflected-wave response is strengthened by a shift toward resonance (Fig. 7): Because of the change in background stratification, c_2 is shifted to be close to the resonance speed, and some of the contribution from the $n = 1$ mode (which is well off resonance) is shifted to the $n = 3$ mode (which is much closer to resonance). The increase between the 3½-layer and 4½-layer solutions is due to the additional contribution of mixed layer shear (the $n = 4$ mode in the linear model), which confines the directly forced currents closer to the surface. With salinity, the fall WJ is strengthened in the eastern ocean, owing to precipitation in the summer and fall: This buoyancy flux weakens, or even eliminates, mixed layer entrainment, thereby thinning the mixed layer even more. Only when the Maldives are included does the semiannual amplitude decrease, due primarily to a weakening of resonance.

The highest solution in our hierarchy, the nonlinear solution to the 4½-layer model with salinity and the Maldive Islands (our “best” solution), compares most favorably with the ship-drift observations (Figs. 1 and 11). We utilize the other solutions in the hierarchy to estimate the relative contributions of the directly forced and reflected-wave responses to this solution. It is sufficient to estimate their contribution to the solution’s mean and semiannual components since they sum to a maximum of 78 cm s^{-1}, accounting for more than 80% of the WJ strength (Fig. 11). The 3½-layer solutions suggest that the semiannual reflected-wave response contributes 25 cm s^{-1} and that the directly forced response (without mixed layer shear) is 41 cm s^{-1}, with 12 cm s^{-1} from the annual mean and 29 cm s^{-1} from the semiannual component. (To estimate the split of the semiannual component into directly forced and reflected-wave parts, we assumed that their amplitude ratio was the same in the nonlinear solution as in the linear one.) The difference in WJ strength between the 3½-layer and 4½-layer solutions measures the contribution of mixed layer shear to the directly forced response; it is 27 cm s^{-1}, with 13 cm s^{-1} and 14 cm s^{-1} from the mean and semiannual components, respectively. The Maldive Islands weaken the semiannual reflected-wave and annual-mean responses by approximately 10 cm s^{-1} and 5 cm s^{-1}, respectively. Overall, then, the reflected-wave response contributes $25 - 10 = 15$ cm s^{-1} to the total (19%), the directly forced response without mixed layer shear contributes to $41 - 5 = 36$ cm s^{-1} (46%), and mixed layer shear provides the remaining 27 cm s^{-1}(35%).

In our best model solution as well as the ship-drift data, the semiannual response is more than twice as large as the annual one, even though the wind components have similar amplitudes (Figs 2c and 2d). One cause is the different structures of the semiannual and annual winds, the more complex structure of the latter generating a weaker oceanic response [section 3a (2i)]. Another is that the semiannual reflected-wave and directly forced parts interfere constructively over much of the interior ocean whereas the annual ones do not, an indication of the semiannual component being near resonance [sections 3a (2ii) and 3b(2)]. Finally, the addition of a mixed layer strengthens the semiannual response but not the annual one, because the shear flow interferes constructively (destructively) with the rest of the response for the semiannual (annual) component [section 3c(3)].

Even in our best solution, the annual component differs considerably from the observed one (Figs. 1c and 11c).

Moreover, it still tends to weaken the fall WJ (and strengthens the spring one) in the central ocean, in contrast to the ship-drift observations in which it has the opposite effect. This discrepancy may result from model deficiencies (e.g., reflected waves are overemphasized, or the directly forced response is too weak), from windage errors in the ship-drift data (section 3d), or from inaccuracies in the winds themselves (section 3e). These results suggest reasons why fall jets are relatively weak in the other models mentioned in the introduction: Either they lack a proper mixed layer, ignore salinity, have no Maldive Islands, or force their models with Hellerman and Rosenstein (1983) winds, which produce a particularly weak fall WJ in the eastern ocean.

In conclusion, by comparing our hierarchy of solutions to the ship-drift climatology, we have been able to assess the importance of various processes in WJ dynamics. Consistent with previous studies, we have confirmed that, although direct forcing accounts for most of the WJ strength, reflected waves and resonance also contribute 19%. In addition, we have demonstrated that precipitation has a major influence on the fall jet through its effect on mixed layer thickness, strengthening it by as much as 30 cm s^{-1} in the eastern ocean. It is likely that further progress in understanding WJ dynamics cannot be made without additional observations. For example, an obvious need is to measure the annual evolution of the mixed layer in the eastern, equatorial ocean. Equally important, given the large discrepancies in existing wind products, more accurate winds are essential.

Acknowledgments

Weiqing Han and Julian McCreary were supported by NSF Grants OCE-92-03916 and OCE-94-16098, and by ONR Contract N00014-97-1-0077. Arthur Mariano was supported by ONR Contract N00014-95-1-0257. We thank Dennis Moore for suggesting improvements to our equatorial damper, and Kevin Kohler for his programming assistance.

REFERENCES

Anderson, D. L. T., and D. J. Carrington, 1993: Modelling interannual variability in the Indian Ocean using momentum fluxes from the UKMO and ECMWF operational weather analyses. *J. Geophys. Res.*, **98,** 12 483–12 499..

— ,— ,R. Correy, and C. Gordon, 1993: The temporal evolution of equatorial currents in the Indian Ocean. Meteorological Office Climate Research Tech. Note 23, Bracknell, Berkshire, United Kingdom, 51 pp. [Available from U.K. Meteorological Office, Bracknell, Berkshire RG12 252, United Kingdom.].

Cane, M. A., 1980: On the dynamics of equatorial currents, with application to the Indian Ocean. *Deep-Sea Res.*, **27A,** 525–544..

— ,and D. W. Moore, 1981: A note on low-frequency equatorial basin modes. *J. Phys. Oceanogr.*, **11,** 1578–1584.. Find this article online

— ,and E. S. Sarachik, 1981: The response of a linear baroclinic equatorial ocean to periodic forcing. *J. Mar. Res.*, **39,** 651–693..

— ,and Y. du Penhoat, 1982: The effect of islands on low-frequency equatorial motions. *J. Mar. Res.*, **40,** 937–962..

Donguy, J. R., and G. Meyers, 1995: Observations of geostrophic transport variability in the western tropical Indian Ocean. *Deep-Sea Res.*, **42,** 1007–1028..

Hellerman, S., and M. Rosenstein, 1983: Normal wind stress over the world ocean with error estimates. *J. Phys. Oceanogr.*, **13,** 1093–1104.. Find this article online

Jensen, T. G., 1993: Equatorial variability and resonance in a wind-driven Indian Ocean model. *J. Geophys. Res.*, **98** (C12), 22 533–22 552..

Knox, R. A., 1976: On a long series of measurements of Indian Ocean equatorial currents near Addu Atoll. *Deep-Sea Res.*, **23,** 211–221..

Kraus, E. B., and J. S. Turner, 1967: A one-dimensional model of the seasonal thermocline. Part II: The general theory and its consequences. *Tellus*, **19,** 98–106..

Legates, D. R., and C. J. Willmott, 1990: Mean seasonal and spatial variability in gauge-corrected global precipitation. *Int. J. Climatol.*, **10,** 111–127..

Legler, D. M., I. M. Navon, and J. J. O'Brien, 1989: Objective analysis of pseudo-stress over the Indian Ocean using a direct-minimization approach. *Mon. Wea. Rev.*, **117,** 709–720.. Find this article online

Levitus, S., and T. P. Boyer, 1994: *World Ocean Atlas 1994.* Vol. 4, NOAA/NESDIS/NODC/OCL, 129 pp..

— ,R. Burgett, and T. P. Boyer, 1994: *World Ocean Atlas 1994.* Vol. 3, NOAA/NESDIS/NODC/OCL, 111 pp..

Mariano, A. J., E. H. Ryan, B. D. Perkins, and S. Smithers, 1995: The Mariano Global Surface Velocity Analysis 1.0. USCG Rep. CG-D-34-95, 55 pp. [Available from RSMAS, University of Miami, 4600 Rickenbacker Cswy., Miami, FL 33149.].

McCreary, J. P., 1985: Modeling equatorial ocean circulation. *Annu. Rev. Fluid Mech.,* **17,** 359–409..

— ,and P. K. Kundu, 1989: A numerical investigation of sea-surface temperature variability in the Arabian Sea. *J. Geophys. Res.,* **94,** 16 097–16 114..

— ,— ,and R. L. Molinari, 1993: A numerical investigation of dynamics, thermodynamics, and mixed-layer processes in the Indian Ocean. *Progress in Oceanography,* Vol. 31, Pergamon, 181–224..

— ,W. Han, D. Shankar, and S. R. Shetye, 1996: Dynamics of the East India Coastal Current 2. Numerical solutions. *J. Geophys. Res.,* **101,** 13 993–14 010..

McPhaden, M. J., 1982: Variability in the central equatorial Indian Ocean. Part 1: Ocean dynamics. *J. Mar. Res.,* **40,** 157–176..

— ,D. V. Hansen, and P. L. Richardson, 1991: A comparison of ship-drift, drifting buoy, and current-meter mooring velocities in the Pacific South Equatorial Current. *J. Geophys. Res.,* **96,** 775–781..

Molinari, R. L., D. Olson, and G. Reverdin, 1990: Surface current distributions in the tropical Indian Ocean derived from compilations of surface buoy trajectories. *J. Geophys. Res.,* **95,** 7217–7238..

Moore, D. W., 1968: Planetary-gravity waves in an equatorial ocean. Ph.D. thesis, Harvard University, Cambridge, MA..

Murtugudde, R., and A. J. Busalacchi, 1998: Salinity effects in a tropical ocean model. *J. Geophys. Res.,* **103,** 3283–3300..

O'Brien, J. J., and H. E. Hurlburt, 1974: An equatorial jet in the Indian Ocean, theory. *Science,* **184,** 1075–1077..

Rao, R. R., R. L. Molinari, and J. F. Festa, 1989: Evolution of the climatological near-surface thermal structure of the tropical Indian Ocean. Part 1: Description of mean monthly mixed-layer depth and sea-surface temperature, surface-current and surface meteorological fields. *J. Geophys. Res.,* **94,** 10 801–10 815..

— ,— ,and — ,1991: Surface meteorological and near-surface oceanographic atlas of the tropical Indian Ocean. NOAA Tech. Memo., ERL, AOML-69, 49 pp..

Reppin, J., F. A. Schott, J. Fishcer, and D. Quadfasel, 1998: Equatorial currents and transports in the central Indian Ocean: Annual cycle and interannual variability. *J. Geophys. Res.,* in press..

Reverdin G., 1987: The upper equatorial Indian Ocean: The climatological seasonal cycle. *J. Phys. Oceanogr.,* **17,** 903–927.. Find this article online

Soloviev, A., R. Lukas, and P. Hacker, 1998: An approach to parameterization of the oceanic turbulent boundary layer in the western Pacific warm pool. *J. Geophys. Res.,* in press..

Sprintall, J., and M. Tomczak, 1992: Evidence of the barrier layer in the surface layer of the Tropics. *J. Geophys. Res.,* **97,** 7305–7316..

Vialard, J., and P. Delecluse, 1998: An OGCM study for the TOGA decade. Part I: Role of salinity in the physics of the western Pacific fresh pool. *J. Phys. Oceanogr.,* **28,** 1071–1088.. Find this article online

Vinayachandran, P. N., 1995: The Bay of Bengal circulation in an OGCM. Ph.D. dissertation, Center for Atmospheric Science, Indian Institute of Science, Bangalore, India, 167 pp. [Available from Center for Atmospheric Science, Indian Institute of Science, Bangalore 560012, India.].

Weller, R. A., M. F. Baumgartner, S. A. Josey, A. S. Fischer, and J. C. Kindle, 1998: A one-year record of atmospheric forcing from the Arabian Sea. *Deep-Sea Res.,* **45,** 1961–1999..

Wyrtki, K., 1973: An equatorial jet in the Indian Ocean. *Science,* **181,** 262–264..

Yoon, J.-H., 1981: Effects of islands on equatorial waves. *J. Geophys. Res.,* **86,** 10 913–10 920..

Tables

Table 1. Values of various constants associated with the linear models. Units are indicated in parentheses. No salinity values are listed for the 2½-layer and 3½-layer models because salinity is neglected in these models. Values for the 4½-layer model without salinity are enclosed in brackets.

Parameter	Notation	Mode number n, layer index i			
		1	2	3	4
		2½-layer model			
Layer thicknesses	H_i (m)	78	278		
Layer temperatures	T_i^* (°C)	27.1	14.2		
Characteristic speeds	c_n (cm s^{-1})	323	134		
Coupling coeffs.	ϕ_n	0.42	0.87		
		3½-layer model			
Layer thicknesses	H_i (m)	77	271	418	
Layer temperatures	T_i^* (°C)	27.2	14.1	9.0	
Characteristic speeds	c_n (cm s^{-1})	375	162	118	
Coupling coeffs.	ϕ_n	0.26	0.71	0.37	
		4½-layer model			
Layer thicknesses	H_i (m)	41 [54]	41 [36]	277 [281]	405 [394]
Layer temperatures	T_i^* (°C)	28.2 [28.2]	27.4 [26.7]	13.7 [13.4]	9.0 [9.0]
Layer salinities	S_i^* (psu)	35.0	35.0	35.4	35.0
Characteristic speeds	c_n (cm s^{-1})	350 [376]	165 [168]	106 [116]	23 [28]
Coupling coeffs.	ϕ_n	0.28 [0.27]	0.91 [0.78]	0.08 [0.15]	1.18 [0.68]

Click on thumbnail for full-sized image.

Figures

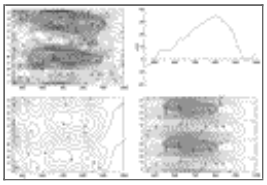

Click on thumbnail for full-sized image.

Fig. 1. Longitude–time plots of equatorial zonal currents U averaged from 1°S to 1°N, determined from the ship-drift climatology of Mariano et al. (1995): The total flow (a: top left) together with its time-averaged mean (b: top right), annual (c: bottom left), and semiannual (d: bottom right) components. The contour interval is 5 cm s^{-1}, and regions where the flow is stronger than 30 cm s^{-1} are shaded. The observations have been smoothed zonally by a 1–2–1 filter. The data is available online at ftp://playin.rsmas.miami.edu/pub/cg.

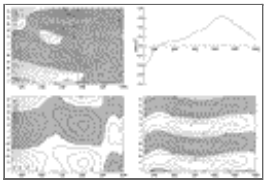

Click on thumbnail for full-sized image.

Fig. 2. Longitude–time plots of equatorial zonal wind stress τ^x averaged from 1°S to 1°N, determined from the FSU pseudostress climatology for the period 1970–96 with ρ_a = 0.001 175 g cm^{-3} and C_d = 0.0015: The total wind (a: top left) together with its time-averaged mean (b:top right), annual (c: bottom left), and semiannual (d: bottom right) components. The contour interval is 0.05 dyn cm^{-2}, and regions of eastward winds (positive values) are shaded.

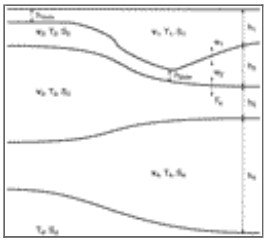

Click on thumbnail for full-sized image.

Fig. 3. A schematic diagram illustrating the layer structure of the 4½-layer model. It consists of four active layers with thicknesses h_i, velocities $\mathbf{v}_i$, temperatures T_i, and salinities S_i, overlying an inert deep ocean with temperature T_d and salinity S_d. Thicknesses h_1 and h_2 are not allowed to be smaller than minimum values, $h_{1\,\min}$ and $h_{2\,\min}$. Water is allowed to transfer between layers with velocities w_1 and w_2.

Click on thumbnail for full-sized image.

Fig. 4. Longitude–time plots of u_1 averaged from 1°S to 1°N for the nonlinear, 2½-layer model, showing the total flow (a: top-left) together with its mean (b: top-right), annual (c: bottom-left), and semiannual (d: bottom-right) components. The contour interval is 5 cm s^{-1}, and regions where the flow is stronger than 30 cm s^{-1} are shaded.

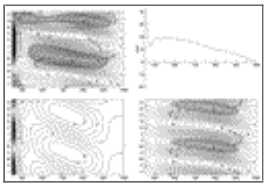

Click on thumbnail for full-sized image.

Fig. 5a. As in Fig. 4 except for the linear, 2½-layer model.

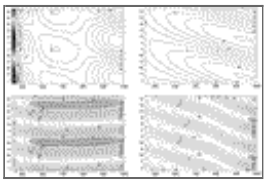

Click on thumbnail for full-sized image.

Fig. 5b. Longitude–time plots of u_1 averaged from 1°S to 1°N for the linear, 2½-layer model, showing the directly forced and reflected-wave responses for the annual component (a: top left and b: top right) and for the semiannual component (c: bottom left and d: bottom right).

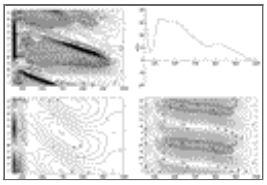

Click on thumbnail for full-sized image.

Fig. 6. As in Fig. 4 except for the nonlinear, 3½-layer model.

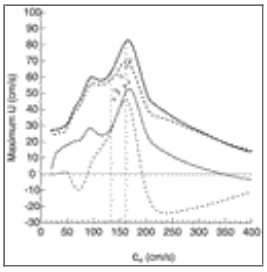

Click on thumbnail for full-sized image.

Fig. 7. Plots of $u_{1\max}$ (thick curve), $u'_{1\max}$ (thin curve), u''_1 (thin-dashed curve), and $\tilde{\mathbf{u}}_{1\max}$ (thick-dashed curve) vs c_n. The four quantities are defined in the text, the first three in section 3b(2) and the fourth in section 3d(2).

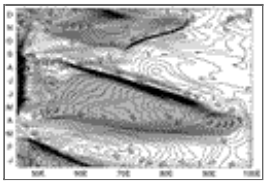

Click on thumbnail for full-sized image.

Fig. 8a. Longitude–time plots of u_1 averaged from 1°S to 1°N for the 4½-layer model without salinity. Both spring and fall WJs are stronger than they are in the 3½-layer solution. The fall jet, however, is still very weak in the eastern ocean (especially east of 85°E).

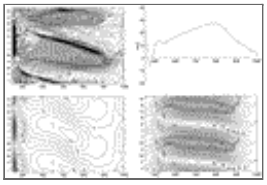

Click on thumbnail for full-sized image.

Fig. 8b. As in Fig. 4 except for the 4½-layer model with salinity. It differs from the solution without salinity (Fig. 8a) primarily in that the fall WJ is enhanced by up to 30 cm s^{-1} in the eastern ocean.

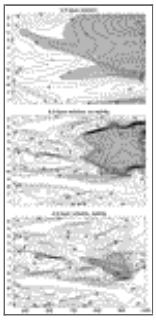

Click on thumbnail for full-sized image.

Fig. 9. Longitude–time plots of equatorial $h_1 + h_2$ for (a) the 3½-layer model, and of equatorial h_1 for the 4½-layer models (b) without salinity and (c) with salinity. All the fields are averaged from 1°S to 1°N. Regions where the fields are thicker than 80 m are shaded. Currents are strengthened in regions where the layer thicknesses are shallow.

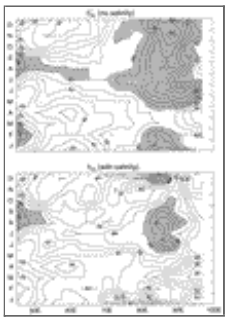

Click on thumbnail for full-sized image.

Fig. 10. Longitude–time plots of equatorial mixed-layer thicknesses estimated from Levitus and Boyer (1994) and Levitus et al. (1994) data in two different ways as described in the text: using temperature only h'_m (a: top panel), and using both temperature and salinity h_m (b: bottom panel). Compare h_m and h'_m with the solutions' thickness fields in the upper two and bottom panels of Fig. 9, respectively. Regions where the fields are thicker than 60 m are shaded.

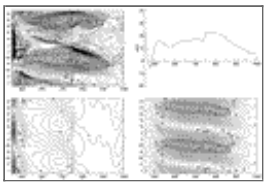

Click on thumbnail for full-sized image.

Fig. 11. As in Fig. 4 except for the 4½-layer model with salinity and the Maldive Islands. In comparison to the solution without the Maldives (Fig. 8b), the spring and the fall WJs have more comparable strengths, the semiannual component is weaker, and the structure of the annual component is altered considerably.

[1] Regrettably, serious errors were introduced into the text of MKM at the time of printing. An erratum can be found after page 248 of *Progress in Oceanography*, 1994, Volume 33, Number 3.

* International Pacific Research Center Contribution Number 12.

[+] Current affiliation: International Pacific Research Center, University of Hawaii, Honolulu, Hawaii.

Corresponding author address: Dr. Weiqing Han, Nova Southeastern University, Oceanographic Center, 8000 N. Ocean Drive, Dania, FL 33004.

E-mail: han@blacktip.ocean.nova.edu

top